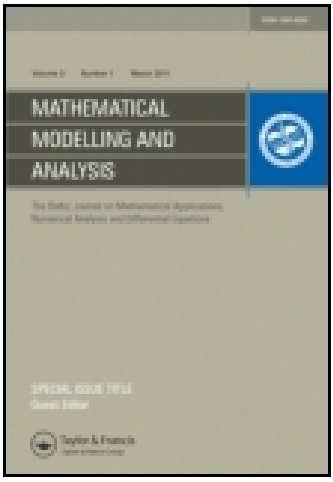

Mathematical Modelling and Analysis

Publication details, including instructions for authors and subscription information:
http://www.tandfonline.com/loi/tmma20

A Full Multigrid Method for Linear Complementarity Problems arising from Elastic Normal Contact Problems

Jing Zhao[a], Edwin A.H. Vollebregt[ab] & Cornelis W. Oosterlee[ac]

[a] Delft University of Technology 2628CD Delft, The Netherlands

[b] VORtech BV 2600AG Delft, The Netherlands

[c] Center for Mathematics and Computer Science 1090GB Amsterdam, The Netherlands E-mails:

Published online: 01 May 2014.

To cite this article: Jing Zhao, Edwin A.H. Vollebregt & Cornelis W. Oosterlee (2014) A Full Multigrid Method for Linear Complementarity Problems arising from Elastic Normal Contact Problems, Mathematical Modelling and Analysis, 19:2, 216-240

To link to this article: http://dx.doi.org/10.3846/13926292.2014.909899

Mathematical Modelling and Analysis
Volume 19 Number 2, April 2014, 216–240
http://dx.doi.org/10.3846/13926292.2014.909899

Publisher: Taylor&Francis and VGTU
http://www.tandfonline.com/TMMA
Print ISSN: 1392-6292
Online ISSN: 1648-3510

A Full Multigrid Method for Linear Complementarity Problems arising from Elastic Normal Contact Problems

Jing Zhao[a], Edwin A.H. Vollebregt[a,b] and Cornelis W. Oosterlee[a,c]

[a] *Delft University of Technology*
2628CD Delft, The Netherlands
[b] *VORtech BV*
2600AG Delft, The Netherlands
[c] *Center for Mathematics and Computer Science*
1090GB Amsterdam, The Netherlands
E-mail(*corresp.*): J.Zhao-1@tudelft.nl
E-mail: edwin.vollebregt@vortech.nl
E-mail: c.w.oosterlee@cwi.nl

Received September 7, 2013; revised March 7, 2014; published online April 15, 2014

Abstract. This paper presents a full multigrid (FMG) technique, which combines a multigrid method, an active set algorithm and a nested iteration technique, to solve a linear complementarity problem (LCP) modeling elastic normal contact problems. The governing system in this LCP is derived from a Fredholm integral of the first kind, and its coefficient matrix is dense, symmetric and positive definite. One multigrid cycle is applied to solve this system approximately in each active set iteration. Moreover, this multigrid solver incorporates a special strategy to handle the complementarity conditions, including restricting both the defect and the contact area (active set) to the coarse grid, and setting all quantities outside contact to zero. The smoother is chosen by some analysis based on the eigenvectors of the iteration matrix. This method is applied to a Hertzian smooth contact and a rough surface contact problem.

Keywords: full multigrid, linear complementarity problems, integral equation, normal contact problems, active set algorithm.

AMS Subject Classification: 65N55; 65R20; 49M30; 35Q74.

1 Introduction

Contact problems in mechanical engineering have been studied and developed for decades. They are concerned with the elastic contact between the surfaces of two bodies. When these are pressed together, a contact area occurs between

them. The challenge is to find this area where the two bodies are in contact and the pressure (normal traction) at the interface. Two complementary conditions are required for the solutions. One states no penetration between the two bodies. This implies the gap between the two surfaces being zero in the contact area but positive outside. The other points out that the pressure is compressive (≥ 0) in the contact area and vanishes outside. This kind of contact problem arises in many industrial branches, such as the investigation of friction and wear [6, 22], rolling contact fatigue [7], and the fatigue life of machine elements [28].

Solving contact problems has been a continuing topic for research, to which Johnson [12] and Kalker [13] contributed with fundamental work. Analytic solutions are only found for some simple contact problems, such as Hertz theory [12]. Fast and efficient numerical solutions are required for more complicated contact problems. The numerical approximations are generally classified into two types. The widely used finite element method (FEM) [15, 16, 36] can be applied for problems involving large deformation and nonlinear materials. Due to the discretization of the whole contacting bodies, however, this method becomes computationally expensive for large problems. The boundary element method (BEM), e.g. [1,17] is efficient for solving homogeneous elastic problems, when assuming small deformations and deformation gradients. This method transforms a 3D boundary value problem into a 2D boundary integral equation and then solves it only at the discrete boundary, which reduces the computational work significantly.

The numerical solvers in the framework of BEM for normal contact problems include Kalker's variational method [13], which is implemented in the CONTACT software [32], and uses Green's functions for the elastic half-space. Particularly, it applies an active set algorithm, called "NORM", to search for the contact area. In each active set iteration, the governing system is solved in the current contact area, which is then modified by the resulting solution. The iterations terminate when all conditions are satisfied. Subsequent to [2], a multigrid strategy for contact problems was developed by Venner and Lubrecht [29], where the complementarity conditions were handled in a distributive smoother and a nonlinear full approximation scheme (FAS), with a multilevel multi-integration (MLMI) technique for matrix-vector products. Another method which combines the MLMI and the conjugate gradient (CG) algorithm for rough contact problems is proposed in [20]. The fast Fourier transform (FFT) technique is also employed, see [25]. A comparison of different methods can be found in [23].

The variational formulation [13] leads to a linear complementarity problem (LCP) with the use of Karush-Kuhn-Tucker (KKT) conditions. Hence, quadratic programming solvers can be applied to the LCP, e.g., the extension of the simplex algorithm, the interior point method, or the active set algorithm [18]. In contact problems, the active set strategy is frequently used, due to its performance and easy mechanical explanation. It has been combined with conjugate gradients [13] and with a multigrid method [29, 39].

The most time-consuming part of the solution procedure for the contact problem is the surface integral, which is a Fredholm integral of the first kind in the prescribed contact area. The discretization of such integral yields a linear

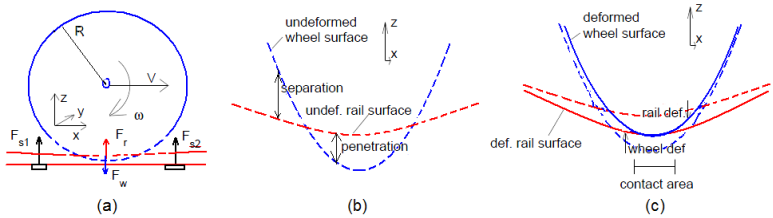

Figure 1. Geometry of contact problems for railway applications [34]: (a) the overall geometry, (b) undeformed state, (c) deformed state.

system with the coefficient matrix being dense, symmetric and positive definite (SPD). Direct methods can be used but not for large problems. A popular iterative method is preconditioned CG [5, 8, 11, 26]. Multigrid is also studied for integral equations of the first kind, see, e.g. [3, 24, 30, 35].

The current state of the art solver for the normal contact problem may be a multigrid method in [29]. However, it is quite involved and nontrivial. The multigrid work here is outlined as follows. In Section 2, the normal contact problem is introduced and the LCP is formulated. Section 3 presents the original active set algorithm "NORM", by Kalker [13]. Section 4 describes the structure of the full multigrid (FMG) method and each component of the multigrid method, particularly the restriction and interpolation to deal with the constraints in the LCP. Two experiments, a Hertzian smooth contact and a rough surface contact, are discussed and solved numerically in Section 5, after which conclusions are summarized. The appendix discusses an approach for generating Gaussian rough surfaces with a given standard deviation.

2 Problem Formulation

This section gives a general description of the normal contact problem, and builds the mathematical model, resulting in the LCP which we will solve using a multigrid method.

2.1 Physics of the normal contact problem

When the surfaces of two bodies roll over each other, a contact area occurs between them, carrying normal and tangential tractions. An elastic field of displacements, strains, and stresses in the bodies appears with these tractions, all of which result in deformations [13]. The tractions and the contact area are the main quantities we solve for. In the *normal contact problem*, the forces of the contacting bodies are perpendicular to the surface [21] and we only consider the normal tractions (pressures) here.

Fig. 1 shows the general geometry of the contacting phenomenon in railway applications. The overall geometry, drawn in Fig. 1(a), displays a wheel rolling on the rail with a forward velocity V and an angular velocity ω. The rail is deformed, caused by the forces from the wheel, F_w, and from the sleepers, F_{s1}, F_{s2}. At the same time, the wheel has deformation due to the force from the

rail, F_r. We stretch this graph vertically in order to have a detailed look at this phenomenon. Figs. 1(b) and (c) show the undeformed and deformed states, respectively. A contact area occurs where the surfaces of the wheel and rail coincide. The distance between their surfaces is positive outside the contact area without any tractions there. Let C denote the contact area and E the exterior area. Then, the *contact conditions* for the normal contact problem are:

$$e(x,y) = 0, \quad p(x,y) \geq 0, \quad \text{for each position } (x,y) \in C, \tag{2.1}$$

$$e(x,y) > 0, \quad p(x,y) = 0, \quad \text{for each position } (x,y) \in E, \tag{2.2}$$

where $p(x,y)$ is the pressure at position (x,y), and $e(x,y)$ is the deformed distance (i.e. gap) between the wheel and rail. Let $h(x,y)$ denote the undeformed distance at (x,y), then the deformed distance, $e(x,y)$, is given by:

$$e(x,y) = h(x,y) + u(x,y), \tag{2.3}$$

where $u(x,y)$ is the deformation. It is assumed that the bodies can not interpenetrate, that the pressure occurs only where the bodies are in contact and that adhesion effects (attraction) are negligible.

2.2 The half-space approach in Kalker's variational approach [13]

The method to calculate the deformation u is based on three simplifying assumptions. First of all, the contact area is very small compared to the two contacting bodies, and hence this area is considered to be *flat*. The second is that the contacting bodies are assumed to be made of homogeneous linear elastic material. The last assumption is to ignore inertial effects in the motion.

These assumptions allow the use of the *half-space approach*, which approximates the elastic field of two contacting bodies considering each body as a *semi-infinite elastic solid* bounded by a plane surface. Based on the classic solutions by Boussinesq and Cerruti (see Johnson [12]) and considering 3D normal contact problems, we give the normal traction-deformation relation, as follows:

$$u^z(x,y) = \iint_C A^{zz}(x,y,\xi,\eta) p^z(\xi,\eta)\, d\xi\, d\eta. \tag{2.4}$$

Here the superscript z denotes the normal direction, u^z and p^z are the normal deformation and pressure, respectively. $A^{zz}(x,y,\xi,\eta)$ is the influence function for normal deformation at the surface position (x,y), due to the contribution of a unit pressure at surface position (ξ,η). This influence function is calculated by:

$$A^{zz}(x,y,\xi,\eta) = \frac{1-\nu}{\pi G}\frac{1}{\rho}, \tag{2.5}$$

where ν is the Poisson ratio, ρ is the distance between points (x,y) and (ξ,η), i.e. $\rho = [(x-\xi)^2 + (y-\eta)^2]^{\frac{1}{2}}$. G is the combined shear modulus of the two contacting bodies, obtained by $\frac{2}{G} = \frac{1}{G_1} + \frac{1}{G_2}$ with G_1 and G_2 being the shear modulus of each body. For two bodies of the same material, we have $G = G_1 = G_2$; in the case of one rigid body, it follows that $G_1 = \infty$, so that $1/G_1 = 0$, and $G = 2G_2$.

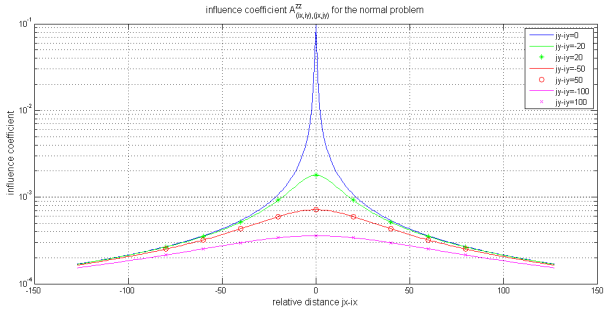

Figure 2. Influence coefficient $A^{zz}_{(ix,iy)(jx,jy)}$ (scaled by G).

2.3 Discretization

Solving contact problems often starts with the discretization of the 2D potential contact area, which is chosen such that it contains the true contact area. The potential contact area is discretized by $mx \times my$ rectangular elements of size $\delta x \times \delta y$. Each element is numbered by (ix, iy) where $1 \leq ix \leq mx$ and $1 \leq iy \leq my$.

The surface pressure p^z in the integral (2.4) is approximated by a piecewise constant function, where the pressure at each element center is used. This means that the integral (2.4) is evaluated by a 2D "mid-point rule". Due to boundary effects, the discrete error of the pressure reduces to $\mathcal{O}(h)$ [13]. The discretization of integral (2.4) yields:

$$u^z_{(ix,iy)} = \sum_{jy=1}^{my} \sum_{jx=1}^{mx} A^{zz}_{(ix,iy)(jx,jy)} p^z_{(jx,jy)}, \tag{2.6}$$

where the subscript (ix, iy) denotes the element. The influence coefficient $A^{zz}_{(ix,iy)(jx,jy)}$ is calculated by integrating (2.5) for a unit pressure in a single element (jx, jy) w.r.t. an observation point (x, y) at the center of element (ix, iy). It has the property that $A^{zz}_{(ix,iy)(jx,jy)} = A^{zz}_{(kx,ky)(lx,ly)}$ when $jx - ix = lx - kx$, $jy - iy = ly - ky$, i.e. the coefficients are identical for pairs of elements that have the same relative distance. Fig. 2 shows an example of the influence coefficients scaled by G (for Test I in Section 5.1).

Denote the total number of elements by $n := mx \cdot my$. If all n elements of the potential contact area are in contact, equation (2.6) leads to:

$$\mathbf{u} = A\mathbf{p}, \quad \mathbf{p}, \mathbf{u} \in \mathbb{R}^n, \ A \in \mathbb{R}^{n \times n}, \tag{2.7}$$

where the influence coefficient matrix, A, is a dense, symmetric and BTTB matrix, i.e. block Toeplitz matrix with Toeplitz blocks.[1] Combining equations (2.3) and (2.7), and considering the discretization of the contact conditions

[1] A Toeplitz matrix is a matrix with each descending diagonal from left to right being constant.

(2.1) and (2.2), we obtain a linear complementarity problem LCP($\mathbf{h}, A$), which aims to find the pressures, $\mathbf{p}$, and contact area, C, satisfying

$$\mathbf{e} = \mathbf{h} + A\mathbf{p}, \tag{2.8}$$

$$e_I = 0, \quad p_I \geq 0, \quad \text{for element } I \in C, \tag{2.9}$$

$$e_I > 0, \quad p_I = 0, \quad \text{for element } I \in E, \tag{2.10}$$

where I is the element index with $I = (iy-1)mx + ix,\ 1 \leq I \leq n$, and E is the exterior area. Note that the constraints on the deformed distance $\mathbf{e}$ are the primary constraints: $e_I = 0$ defines the active set, i.e. contact area, and $e_I > 0$ are inactive constraints, i.e. the exterior area. This LCP represents a mathematical model for the normal contact problem.

Noticing the nice regular BTTB structure of the coefficient matrix A in (2.7), one may think that fast Toeplitz solvers or solvers based on the FFT can be used. This is however generally not directly true because of the additional constraints. We do not allow any solution p, but require $p = 0$ in the exterior area E. Setting $p_I = 0$ for $I \in E$ removes the corresponding rows and columns from matrix A and destroys the BTTB structure. Solvers for a BTTB matrix are not considered in this paper.[2] According to condition (2.9), we have $\mathbf{e} = \mathbf{h} + A\mathbf{p} = \mathbf{0}$ in the contact area C, and thus:

$$A\mathbf{p} = -\mathbf{h}, \quad \text{in } C, \tag{2.11}$$

which is the main system to be solved. We will discuss the original method and the FMG method for solving the LCP in the sections to follow.

3 Original Method: Active Set Algorithm

The active set algorithm is well-known for optimization problems, such as the LCP above. The main idea is to partition the computational domain into two groups, i.e. *active and inactive sets*. Those parts that satisfy the constraints are put in the active set and the others are in the inactive set. Only the active set is considered when solving the equality problem. One active set iteration has two steps, i.e. first determine a current active set as the working set, and then solve the equality problem in this active set. These two steps are repeated until all constraints are satisfied [18].

The convergence rate of the active set algorithm depends on the concrete problems to be solved. In contact problems, generally 5 to 15 iterations are required [33]. The contact area is part of the potential contact region and regarded as the active set, and the exterior area is the inactive set. The original algorithm "NORM" by Kalker [13] starts with an initial contact area, in which the undeformed distance is less or equal to zero. The conjugate gradient (CG) method (without preconditioner) is applied to solve the linear system (2.11) in the current contact area. The results are used to determine an updated contact area, according to conditions (2.9) and (2.10). Such process is repeated until

[2] An algorithm that does exploit the structure of the BTTB matrix using FFT's is presented in [33]. The combination of this with MG method will be investigated in our future work.

the contact area converges. The reason why no preconditioner is applied with CG for the integral equation lies in the fact that the matrix is rather well-conditioned, and CG converges rapidly.

We have to solve a linear system (2.11) in each active set iteration. This system is large and has a dense system matrix. Several active set iterations are needed before the correct contact area is obtained, which means that we have to solve many such systems.

4 A Full Multigrid Method (FMG)

This section presents the FMG method for the LCP (2.8)–(2.10). We start with an "MG+active set" algorithm, which inserts a multigrid solver into an active set iteration. Each component of the multigrid solver is detailed here. The MG+active set algorithm is incorporated in a nested iteration technique, resulting in the FMG method.

4.1 MG+active set algorithm

When examining the contact conditions, there is no need for exact values of deformed distance $\mathbf{e}$ or pressures $\mathbf{p}$, since the conditions only depend on whether values are positive, negative or zero.[3] Therefore, in each active set iteration, we can solve system (2.11) *approximately*, by only one multigrid cycle. This yields an *MG+active set algorithm*, which is described as follows:

1. Start with some grid discretization for the potential contact area. Check undeformed distance $\mathbf{h}$: put element I satisfying $h_I \leq 0$ in the initial contact area C^0.
2. Set the pressures in the exterior area E^k to zero, and define the system (2.11) in the current contact area C^k.
3. Apply one multigrid cycle to this system, resulting in the approximate pressures $\mathbf{p}$, and compute the deformation $\mathbf{u} = A\mathbf{p}$.
4. Check the contact conditions:
   (4.a) Consider each element I in the contact area C^k: if pressure $p_I < 0$ then put element I into the exterior area, and set $p_I = 0$. This leads to the contact area $\overline{C}^{k+1}$ and exterior area $\overline{E}^{k+1}$.
   (4.b) Consider each element I in the exterior area $\overline{E}^{k+1}$: put element I into the contact area C^{k+1} with its deformed distance $e_I = h_I + u_I \leq 0$. Now, a new contact area C^{k+1}, and exterior area E^{k+1}, have been obtained.
5. If this updated contact area C^{k+1} is different from the previous area C^k, then go to step 2. If not, go to step 6.
6. If the solution is not of the required accuracy, then go to step 2. Otherwise, stop since we have found the converged contact area and the pressures on it.

[3] For a conjecture on the convergence of "NORM", see [31].

The multigrid method plays a crucial role in this algorithm. We will give more details about its components in the following subsection.

4.2 Multigrid components

The multigrid method is one of the most efficient numerical solvers, especially for systems of equations arising from elliptic PDEs. But here we will use the multigrid algorithm to deal with system (2.11), which arises from an integral equation and is governed by a dense coefficient matrix, in an active set iteration. Moreover, the complementarity conditions should be taken into consideration.

A two-grid algorithm is given below. It is easy to be extended to a multigrid algorithm. The subscripts h and H are the mesh sizes, denoting the fine and coarse grid, respectively.

1. *Pre- and post- smoothing*: We use the damped Gauss–Seidel method as the smoother. Notice that we only deal with the pressures within the contact area C_h^k, because the pressures in the exterior area E_h^k are fixed to zero.
2. *Calculate defects*: The defects in the contact area, C_h^k, are computed, and the defects in the exterior area E_h^k are set to zero. This gives us the fine grid defects, $\mathbf{d}_h$.
3. *Restrict* the defects, $\mathbf{d}_h$, and the contact area, C_h^k, to the coarse grid, resulting in coarse grid defects, $\mathbf{d}_H$, and a coarse contact area, C_H^k, respectively.
4. *On the coarse grid*: Apply an exact solver, e.g. a Gauss elimination method, for the defect equation, $A_H\overline{\mathbf{v}}_H = \mathbf{d}_H$, defined by the coarse contact area, C_H^k. The coarse grid correction, $\mathbf{v}_H$, is set as: $\mathbf{v}_H = \overline{\mathbf{v}}_H$ in C_H^k, and $\mathbf{v}_H = 0$ in E_H^k.
5. *Interpolate* the coarse grid correction $\mathbf{v}_H$ to the fine grid, yielding the fine grid correction $\mathbf{v}_h$, then set $\mathbf{v}_h = 0$ in the exterior area E_h^k.
6. *Correction*: Add correction $\mathbf{v}_h$ to the pressures $\mathbf{p}_h$ for all elements in the potential contact area.

The difference between this algorithm and the standard multigrid method is that not only the defects $\mathbf{d}_h$ but also the contact area C_h^k (active set) are restricted to the coarse grid. The resulting area C_H^k defines the defect equation on the coarse grid. In order to satisfy the condition that $p_I = 0$ in the exterior area, all quantities including the pressure, defects, corrections in the exterior areas, E_h^k and E_H^k, are set equal to zero in this algorithm.

The idea for coarsening is the simple and the most frequently used choice, *standard coarsening*, i.e. doubling the element size in each direction ($H = 2h$). An example is depicted in Fig. 3, where all elements are numbered in lexicographic ordering. The restriction and interpolation operators are described based on the shadow elements in Fig. 3. The details are as follows, where the formulas in the first and the third items are used for the elements in both contact and exterior areas.

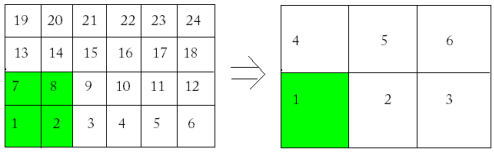

Figure 3. Standard coarsening means combining 2×2 cells into one coarse grid cell. For example, the shadow element 1 on the coarse grid (on the right) is obtained by combining four shadow elements 1,2,7,8 on the fine grid (on the left).

1. Restriction of the defects: we apply the "four-point average", a frequently used restriction approach on cell-centered meshes. Take the shadow elements in Fig. 3 as an example, we have $d_H^1 = \frac{1}{4}(d_h^1 + d_h^2 + d_h^7 + d_h^8)$, where the superscripts denote the element numbers.
2. Restriction of the contact area: among the elements 1, 2, 7, 8, if there is at least one element in the contact area C_h, then the coarse grid element 1, which is obtained by combining these four elements, is put in the coarse contact area C_H.
3. Interpolation of the correction: we "copy" the correction of coarse element 1, i.e. v_H^1, to the correction of the four corresponding fine grid elements, 1, 2, 7, 8, i.e.: $v_h^1 = v_h^2 = v_h^7 = v_h^8 = v_H^1$. This seemingly very basic interpolation is consistent with the restriction approach of the contact area, and appears to be a robust choice for the irregular and possibly tiny contact regions encountered in the rough contact problem, discussed below.

4.3 The FMG scheme

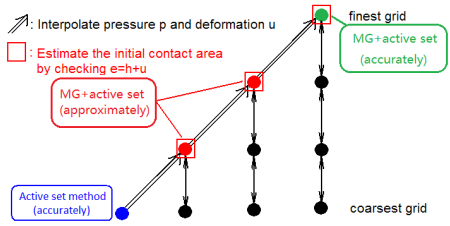

Figure 4. The FMG scheme.

It is well known that an accurate initial guess can accelerate the convergence. This is even true for the contact problem where we must also identify the active contact region. Therefore, the MG+active set algorithm is combined with nested iteration, which aims at providing an improved initial contact area and pressure for the target grid. This leads to the FMG method. Fig. 4 illustrates its structure, where each circle denotes a grid level. The method is described as follows:

1. We start on the coarsest grid, where the LCP is solved accurately by an active set algorithm. In other words, we use a direct solver for the governing integral equation.
2. Solving the LCP results in a contact area C, pressure $\mathbf{p}$, and the deformation $\mathbf{u}$ where $u_I = -h_I$ for $I \in C$. The pressures $\mathbf{p}$ and deformations $\mathbf{u}$ are interpolated to a finer grid. The interpolation strategy of the former is the "copy" strategy discussed before. For the latter, we use bi-linear interpolation.
3. On the finer grid:

   (3.a) Obtain an initial contact area based on the deformed distance $\mathbf{e}$, calculated by $\mathbf{e} = \mathbf{h} + \mathbf{u}$, where the undeformed distance $\mathbf{h}$ can be computed on this grid level. All the elements I for which

   $$e_I \leq \beta \max(\mathbf{u}), \tag{4.1}$$

   are put into an initial contact area, with β a tolerance parameter.

   (3.b) The LCP on this grid level is solved by several iterations of the MG+active set algorithm, until the contact area does not change anymore.
4. Repeat steps 2 and step 3 until we reach the target grid, where the MG+active set algorithm is applied to solve the final contact area, and the pressures to the required accuracy here.

In this FMG algorithm, the LCPs on intermediate grids are only solved approximately, which gives a converged contact area, but the pressures do not need to be of required accuracy. The converged contact area is "interpolated" to the finer grid, based on the deformed distance. This appears sufficient for an improved initial pressure and contact area on target grid in the numerical tests as seen in Section 5.

4.4 Some analysis on Jacobi and Gauss–Seidel smoothers

Since Jacobi and Gauss–Seidel (GS) relaxations are often used as smoothers in multigrid for elliptic PDEs, we study them for our integral problem here. For simplicity, a 2D problem is built: we consider a cylinder of infinite length, rolling on a flat surface. Then, the contact area can be defined as $[-\alpha, \alpha]$ in x-direction and "$[-\infty, \infty]$" in y-direction. Thus, we focus on the pressure distribution in x-direction, leading to a 2D problem. We take the contact area to be $[-2.56, 2.56] \times [-500, 500]$ mm^2, which is discretized by a 32×1 grid. The resulting matrix A is dense, symmetric and Toeplitz.

Fig. 5(a) presents the eigenvalues of the Jacobi iteration matrix. As can be seen, there is one eigenvalue far away from 1. This causes multigrid divergence as the coarse grid correction might fail to reduce the component enlarged so much. Damping by a very small parameter may shift it towards 1, but then the correction to the solution in each iteration will be very small, making the convergence slow. On the other hand, most eigenvalues are around 0.9. This

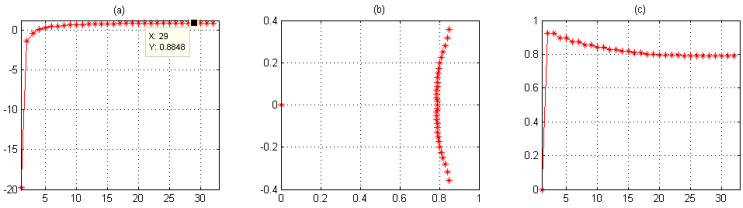

Figure 5. (a) the eigenvalues of the Jacobi (no damping) iteration matrix. (b) the eigenvalues of the (undamped) Gauss–Seidel iteration matrix, their absolute values are given in (c).

implies inefficiency to eliminate the related eigenvectors. Hence, Jacobi as a smoother for MG in our method is rejected.

Fig. 5(b) shows the eigenvalues of the GS iteration matrix in the complex plane. The absolute eigenvalues are given in (c). All eigenvalues are bounded by 1, implying that GS is a convergent solver.

The spectral radii of Jacobi and GS for this integral equation are relatively large. A dense coefficient matrix A for the integral equation [29] implies global (i.e. nonlocal) dependence in the system. During relaxation, updating the pressure at one point results in changes of the deformations at all other points. These deformations accumulate, which influences the efficiency of the Jacobi and GS relaxations.

To understand whether GS can be a smoother in MG for our problem, one may suggest to apply the local Fourier analysis (LFA). This technique is however based on the assumption that the relaxation is a local process, i.e. updating each unknown uses the information from only a few neighbors. However, this is not the case for our problem, where the information on all elements in contact is needed to update one unknown, since each entry of the original coefficient matrix is non-zero. Moreover, Fourier modes fail to resemble the shape of the eigenvectors of the iteration matrix of this integral equation. We will therefore only check with the help of the *eigenvectors* and *eigenvalues* of the iteration matrix for the smoothing efficiency.

Fig. 6(a) shows the error $|\mathbf{e}^i| = |\mathbf{p} - \mathbf{p}^i|$ after the ith GS iteration, where $i = 0, 10, 20$ and $\mathbf{p}$ is the exact solution. As expected, the error gets smoother after more relaxations. The error $\mathbf{e}$ can be expressed as a linear combination of the eigenvectors, i.e. $\mathbf{e} = \sum_j c_j \mathbf{v}^j$. We plot these c_j coefficients in Fig. 6(b) for the three errors in (a). As can be seen, when the error becomes smooth after 20 iterations, the coefficients for most eigenvectors are almost zero, except for the coefficients $c_j, j = 2, \ldots, 9$.

Figs. 7(a)–(d) exhibit in red dots the corresponding eigenvectors. Because of the conjugate property of GS eigenvalues in Fig. 5(b), the pairs of eigenvectors have symmetric shape. So we do not show them here. These modes are smooth. They correspond to the large eigenvalues in Fig. 5(c). The small eigenvalues are connected to eigenvectors with complicated shapes, e.g., $\mathbf{v}_h^{18}$ and $\mathbf{v}_h^{32}$ in Figs. 7(e) and (f), respectively. Therefore, similarly to the high- and low-frequency Fourier modes, we can also separate the eigenvectors into

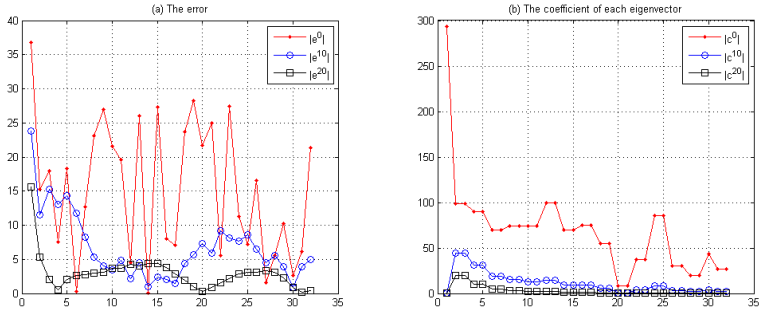

Figure 6. GS: (a) shows the error $|\mathbf{e}^i| = |\mathbf{p} - \mathbf{p}^i|$ after i GS iterations ($i = 0, 10, 20$), where $\mathbf{p}$ and $\mathbf{p}^i$ are the exact solution and the iterates, respectively. The error can be expressed as $\mathbf{e} = \sum_j c_j \mathbf{v}^j$, $j = 1, \ldots, 32$, where $\mathbf{v}^j$ is the jth eigenvector of the iteration matrix, with coefficients c_j giving the contribution of this eigenvector to the error. These coefficients are stored in one vector $\mathbf{c}$, shown in (b) for different errors $\mathbf{e}^i$ in (a).

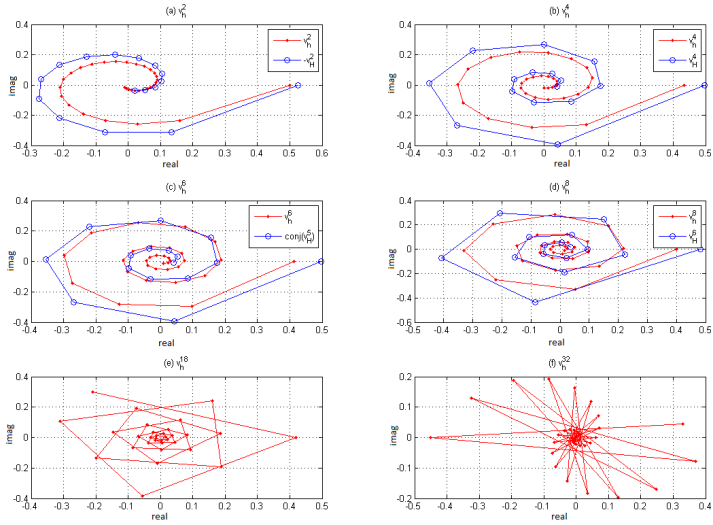

Figure 7. GS: The eigenvectors $\mathbf{v}_h^i$ with $i = 2, 4, 6, 8, 18, 32$ are given in red dots in the complex plane, h denotes the fine grid 32×1. The blue circles shows the corresponding eigenvectors of GS on coarser 16×1 grid.

rough and smooth modes, where the former can be reduced by the smoother efficiently, and the latter remain after smoothing.

A question is, whether the smooth modes $\mathbf{v}_h^i$ with $i = 2, 4, 6, 8$ can be represented on a coarser grid. Figs. 7(a)–(d) gives in blue circles the eigenvectors on a 16×1 grid, that have similar shapes as the fine grid smooth modes. We see that the fine grid smooth modes that can not be reduced efficiently, can be represented on the coarse grid, where they look rougher and can be reduced efficiently.

This shows numerically that GS may be a satisfactory smoother for our

integral problem.

5 Numerical Experiment and Results

In this section, we perform two numerical experiments, on a smooth and on a rough surface, respectively. We start by selecting a smoother and its damping parameter for the MG solver. Then, three V-cycles are compared. The performance of the MG+active set algorithm and the FMG method are investigated, comparing with the original method. The efficiency of interpolation and restriction of the active set is also discussed.

The stopping criteria is chosen as

$$\|r\|_{rms}/\|h\|_{rms} \leq 10^{-6}, \tag{5.1}$$

where r is the defect, and the root-mean square error is $\|\cdot\|_{rms} = \|\cdot\|_2/\sqrt{n}$, with n the number of unknowns. Moreover, a 4×4 grid is used as the coarsest grid. We begin with the smooth contact surface experiment.

5.1 Test I: Hertzian smooth contact

The first test is a "Hertzian" case [12]. The undeformed distance function reads

$$h(x,y) = \frac{1}{2R_x}x^2 + \frac{1}{2R_y}y^2 - \delta,$$

where $R_x = 300$ mm and $R_y = 163$ mm are the principal relative radii of curvature, and $\delta = 0.1091$ mm is the maximum inter-penetration of the undeformed profiles. The potential contact area is $(x,y) \in [-10,10] \times [-6,6]$ mm^2. Steel material with shear modulus $G = 82000$ N/mm^2 and Poisson ratio $\nu = 0.28$ is used to calculate the coefficient matrix A in system (2.11). We solve for the contact area, C, and the corresponding pressures, $\mathbf{p}$.

An analytic solution to this normal contact problem is given in [12]. The contact area is elliptic. For steel material in this test problem, the semi-axes of the contact ellipse are $a = 6.0$ mm, $b = 4.0$ mm, where a and b are half widths of the contact ellipse in the x- and y-directions, respectively. The normal pressure is zero outside the contact ellipse. In the contact area, it has "semi-ellipsoidal" form:

$$p_n(x,y) = p_{max} \cdot \sqrt{1 - \left(\frac{x}{a}\right)^2 - \left(\frac{y}{b}\right)^2},$$

where the maximum pressure, $p_{max} = 3F_n/(2\pi ab) = 1631$ N/mm^2, with total load $F_n = 82000$ N.

5.1.1 Results by the multigrid solver

First, we analyze the multigrid solver numerically to determine the efficiency of the multigrid components. The system we solve here is the C^0 *system*, which is (2.11) defined on the initial contact area C^0. In this test, the C^0 system will be solved to a high accuracy given by (5.1).

As analyzed before, the Jacobi relaxation is not a good smoother for MG, particularly not when a fine discretization is used. Moreover, the damped Jacobi and red-black GS also exhibited worse convergence. We therefore do not show these results here.

The Gauss–Seidel relaxation with underrelaxation is required. To verify this, we tried damped GS smoother with $\omega = 0.8$, $\omega = 1$ (standard GS) and $\omega = 1.1$ (SOR). The iteration numbers and convergence factors are given in Table 1 for two discretization resolutions. The convergence factor is defined as in [27]: $\widehat{q}^{(m)} = \sqrt[m]{\frac{\|d_h^m\|_{rms}}{\|d_h^0\|_{rms}}}$. Quantity $\widehat{q}^{(m)}$ is an average defect reduction factor over m iterations, so it may be an accurate estimate for the multigrid convergence, if m is sufficiently large. The smaller the convergence factor is, the better the convergence performance. In our tests, m is chosen to be the total number of iterations when the desired accuracy is achieved.

Table 1. Hertzian contact: The number of V(1,1)-cycles by multigrid with GS smoothers to solve C^0 system. The convergence factors of multigrid are given in brackets.

Discretization	$\omega = 0.8$	$\omega = 1$	$\omega = 1.1$
64×64	9 (0.19)	9 (0.20)	10 (0.24)
128×128	9 (0.20)	10 (0.24)	11 (0.28)

From Table 1, we find that the GS method with $\omega = 0.8$ is a fine choice, since its convergence factor is the smallest and it requires only 9 iterations on a 128×128 grid. In [29], Jacobi and Gauss–Seidel were regarded as unstable smoothers. However, the latter with underrelaxation works well for our integral problems. Hence, we will use GS with $\omega = 0.8$ as the smoother in our multigrid method.

Remember that in our MG solver also the contact area is restricted to the coarse grid. The results in the table imply that this special strategy is efficient and seem to result in a mesh-independent solver.

5.1.2 Results by the MG+active set algorithm

We arrive at the analysis of the MG+active set algorithm to solve the LCP (2.8)–(2.10). Three V-cycles, V(1,1), V(1,0) and V(0,1) cycles, are implemented in the MG+active set algorithm. Table 2 shows the numbers of active set iterations by MG+active set algorithm (one active set iteration is combined with one MG cycle) and by the original method. As can be seen the former requires slightly more active set iterations than the latter. Moreover, the iteration numbers increase as the problem gets larger by the two methods.

However, the dominant effect of the computational time is the total number of matrix-vector products (MVPs). Therefore, we make a comparison on this between the MG+active set algorithm and the original method. In our algorithm, the damped GS smoother can be regarded as one MVP. Hence, one V(1,1)-cycle calculates three MVPs on each grid level (except for the coarsest grid, where the cost can be ignored): one for both pre- and post-smoothing, and one to compute the defect. Similarly, V(1,0)- and V(0,1)-cycles have two

Table 2. Hertzian contact: the total number of active set iterations by MG+active set algorithm and the original method, with the numbers of work units in brackets.

Discretization	V(1,1)	V(1,0)	V(0,1)	Active set+CG
32×32	9 (35)	15 (39)	15 (39)	5 (74)
64×64	9 (36)	16 (43)	16 (43)	7 (123)
128×128	10 (40)	18 (48)	16 (43)	8 (182)
256×256	12 (48)	21 (56)	20 (53)	9 (260)

Table 3. Hertzian contact: the total number of active set iterations by FMG on the target grid and by the original method, with the numbers of work units in brackets.

Discretization	V(1,1)	V(1,0)	V(0,1)	Active set+CG
32×32	6 (24)	13 (36)	13 (36)	5 (74)
64×64	6 (27)	11 (32)	11 (32)	7 (123)
128×128	5 (23)	9 (27)	8 (24)	8 (182)
256×256	7 (34)	9 (29)	7 (24)	9 (260)

MVPs on each grid level. The size of an MVP reduces by a factor 4 when going to a next coarser grid. Let the cost for one MVP on the target grid to be one *work unit*. Then, total numbers of work units are rounded and given in brackets. It can be found that the V(1,1)-cycle requires fewer MVPs than the other two V-cycles.

As a comparison, the numbers of work units by the original method are also shown in this table, where one MVP is implemented in each CG iteration. We can find that the MG+active set algorithm shows a great reduction of the number of work units compared with the original method.[4]

5.1.3 Results by the FMG method

Now, we combine the MG+active set algorithm with the FMG technique, where we choose $\beta = 0.003$ in Eq. (4.1) to determine the initial contact area on finer grids, and present the convergence results in Table 3. We find that the numbers of active set iterations on the target grid are fewer when the FMG technique is used, comparing with the results in Table 2. Moreover, these numbers stay stable or even decrease as the problem size gets larger.

The numbers of work units are given in brackets. FMG presents a significant reduction of work units comparing with the original method shown in the last column of this table. Among these three V-cycles, V(0,1)-cycle has the smallest cost for the larger problem 256×256.

A comparison is made of the difference between the initial contact area and the converged contact area when solving on the 32×32 grid, which is shown in Fig. 8, where the black dots denote the elements in the contact area and yellow represents the exterior area. The V(1,1)-cycle is used in the FMG method.

[4] Note that MVPs have complexity $\mathcal{O}(n \log n)$ if FFTs can be applied, but are $\mathcal{O}(n^2)$ if this is not the case.

Table 4. Hertzian contact: The norm $\|\mathbf{p}-\mathbf{p}_h^{FMG}\|_{rms}$. The first column is the number of iterations, where 0 indicates the initial error. $h=\max(h_x,h_y)$ is the maximum mesh size. "(C)" means that after this iteration, the contact area is modified, and "–" means that the numerical error does not change.

The V(1,1)-cycle is used in FMG.

Discretization	8×8	16×16	32×32	64×64	128×128	256×256
h	2.5	1.25	0.625	0.3125	0.1563	0.0781
0	315.19	239.54	142.09	78.97	41.04	22.84
1	56.73	81.92 (C)	44.12 (C)	17.51 (C)	8.14 (C)	10.00 (C)
2	44.90	33.73	18.57 (C)	7.63	4.55 (C)	4.07 (C)
3	–	28.31	16.74	6.82	3.67 (C)	2.36 (C)
4	–	–	–	–	–	1.97 (C)
5	–	–	–	–	–	–
$\|\mathbf{p}-\mathbf{p}_h\|_{rms}$	45.29	27.69	16.59	6.77	3.70	1.97

It can be seen from the figure that the initial contact area, using the FMG scheme (in (b)) resembles better the converged contact area (in (c)), than the initial contact area (in (a)) based on the original approach using the undeformed distance. This implies that, the approach to "interpolate" the contact area, based on the deformed distance, is efficient in this case.

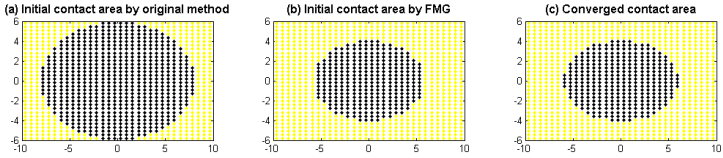

Figure 8. Hertzian contact: contact areas on a 32×32 grid: (a) the initial contact area obtained by the original method, selecting all the elements I with $h_I\le 0$, (b) the initial contact area by the FMG scheme, (c) the converged contact area.

5.1.4 FMG and the discrete error

The FMG method has the interesting property that it can achieve the discrete error after several MG iterations on the target grid. Here, we also check this property for our problem and our FMG method. For different grid scenarios, Table 4 shows the discrete error $\|\mathbf{p}-\mathbf{p}_h\|_{rms}$ and the numerical error after the kth MG iteration on the target grid ($k=0,1,\ldots,5$). $h=\max(h_x,h_y)$ is the maximum mesh size. "(C)" indicates that after this iteration, the contact area is modified, and "–" means that the numerical error does not change.

As can be seen, $\|\mathbf{p}-\mathbf{p}_h\|_{rms}$ for different discretization gives $\mathcal{O}(h)$ accuracy of the pressure, which is also indicated in [13]. FMG achieves the discrete error after a few iterations. Then, more MG iterations do not help to reduce the discrete error. Moreover, for the 256×256 problem, the error already reaches the discrete error even when small modifications of contact area are still to be made.

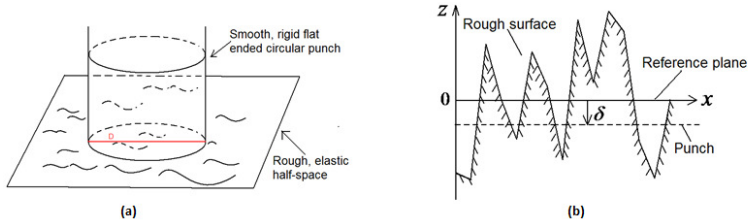

Figure 9. (a) The general profile of rough surface contact; (b) Undeformed state in 1D situation.

5.2 Test II: Rough surface contact

We implemented a problem of friction-less contact between a smooth, rigid flat ended circular punch and a rough, elastic half-space, see also [14]. Fig. 9(a) shows a general profile of this problem. The data are given, as follows:

- Potential contact area: $[-6, 6] \times [-5, 5]$ mm^2.
- Diameter of the punch: $D = 8.97$ mm.
- Decay factor: $\gamma = 0.8$.
- Material parameters of the rigid punch: $G_1 = E_1 = \infty$.
- Material parameters of the half-space: ν_2=0.28 (steel), E_2=1.02×10^5 N/mm^2, G_2=$E_2/[2(1+\nu_2)]$ = 40000 N/mm^2.
- Coefficient of friction: $\mu = 0$.

In a friction-less contact with an elastic solid, the contact stresses only depend on the shape of the gap between the two contacting bodies before loading, i.e. on the undeformed distance [12]. Fig. 9(b) gives the configuration in a 1D situation, where the reference plane coincides with $y = 0$, since the mean of the surface heights, generated by the method discussed in the appendix, is equal to zero. According to this figure the undeformed distance h can be calculated, as follows:

$$h(x,y) = \begin{cases} -[z(x,y) + \delta], & \text{when } x^2 + y^2 \le (D/2)^2, \\ \infty, & \text{otherwise,} \end{cases}$$

where δ is the penetration, which is negative when the punch is above the reference plane and positive below the reference plane.

The rough surface generated in Fig. 12(b) in the appendix is used. For the FMG algorithm, the surface height on each grid level is computed. Fig. 10 presents the surfaces on four successive grids, showing similar shapes.

The experiments are implemented for the Cases 1, 2, 3 with δ equal to -0.11 mm, 0.01 mm and 0.01 mm, respectively. The penetration δ governs the percentage of the actual contact area w.r.t the surface of the punch, which is 5.0%, 12.0% and 28.2% in Cases 1–3, respectively.

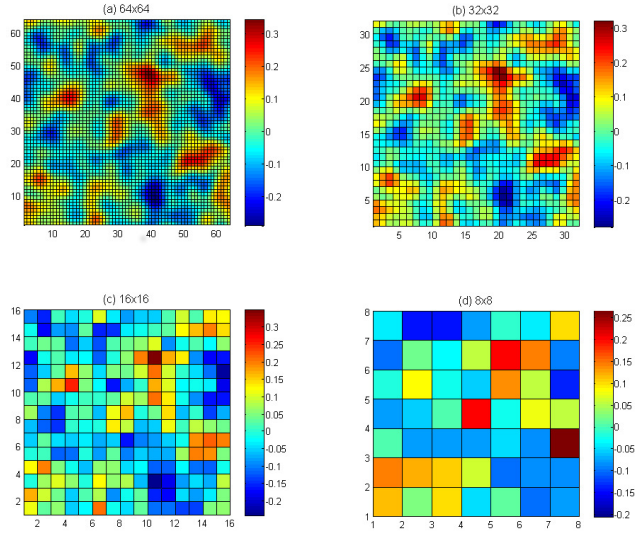

Figure 10. The rough surfaces for four successive grids. They indicate similar shapes.

Table 5. Rough contact Case 1: the total number of active set iterations by FMG and the original method, with the numbers of work units in brackets.

Case 1: $\delta = -0.11$, 5.0% contact				
Discretization	V(1,1)	V(1,0)	V(0,1)	Active set+CG
32×32	7 (32)	14 (40)	14 (39)	3 (35)
64×64	7 (31)	14 (40)	14 (40)	5 (69)
128×128	7 (31)	14 (40)	14 (41)	6 (112)
256×256	7 (32)	13 (39)	13 (39)	8 (167)

5.2.1 Results by FMG

Table 5 gives the total number of active set iterations by FMG on the target grid, and by the original method to solve Case 1. FMG has fewer iterations than the MG+active set algorithm, the results of which are not shown here. As can be seen from the table, FMG does not show a superiority compared to the original method when considering the iteration numbers. However, as expected, a reduction of work units by FMG is found. Moreover, as the problem size gets larger, the number of work units increases for the original method whereas it stays stable for the FMG method. The V(1,1)-cycle requires somewhat fewer work units than the other two cycles for each problem size.

The results in Tables 6 and 7 for Case 2 and Case 3, respectively, show the same behavior. Comparing these three cases, the work units by the original method grows as the penetration δ increases, i.e. as more elements come in contact. However, FMG shows stable work units for the three cases.

The above comparison shows inefficiency of the original method, which solves the system in each active set iteration to high accuracy by CG. One

Table 6. Rough contact Case 2: the total number of active set iterations by FMG and the original method, with the numbers of work units in brackets.

Case 2: $\delta = 0.01$, 12.0% contact				
Discretization	V(1,1)	V(1,0)	V(0,1)	Active set+CG
32×32	7 (31)	13 (36)	13 (36)	4 (57)
64×64	8 (36)	14 (40)	15 (43)	5 (90)
128×128	8 (36)	14 (41)	14 (41)	8 (148)
256×256	7 (33)	12 (37)	12 (38)	8 (221)

Table 7. Rough contact Case 3: the total number of active set iterations by FMG and the original method, with the numbers of work units in brackets.

Case 3: $\delta = 0.25$, 28.2% contact				
Discretization	V(1,1)	V(1,0)	V(0,1)	Active set+CG
32×32	8 (35)	14 (40)	15 (42)	5 (72)
64×64	8 (37)	15 (45)	14 (42)	6 (107)
128×128	7 (34)	13 (39)	14 (42)	8 (169)
256×256	7 (35)	12 (38)	12 (38)	9 (244)

Table 8. Case 3: the total number of active set iterations by inaccurate CG, with the numbers of work units in brackets. The second row is the number of CG iterations in each active set iteration.

Case 3: $\delta = 0.25$, 28.2% contact					
#it	20	15	10	5	4
32×32	5(110)	5(85)	5(60)	6(42)	7(42)
64×64	6(132)	6(102)	6(72)	8(56)	10(60)
128×128	8(176)	8(136)	8(96)	11(77)	14(84)
256×256	9(198)	9(153)	10(120)	15(105)	DIV

may solve the system approximately by several CG iterations (i.e. to replace one-MG cycle by a small number of CG iterations) We show the results for Case 3 in Table 8, where the second row "#it" is the number of CG iterations in each active set iteration. We find that a larger number of active set iterations are needed when fewer CG iterations are used. Divergence even occurs when only four CG iterations are used to modify the active set for a 256×256 problem. Comparing with Table 7, this method requires fewer work units than the original method, but still more than the FMG method.

Fig. 11 displays the contact areas obtained on a 32×32 grid for these three cases, where the ith row denotes the Case i, $i = 1, 2, 3$. The first and second columns are the initial contact areas obtained by the original method and by FMG with a V(1,1)-cycle, respectively. The last column gives the converged contact area in each case. It can be seen again that the initial contact areas, obtained by the FMG scheme resemble much better the converged contact areas, than those obtained by the original method for these three cases. It

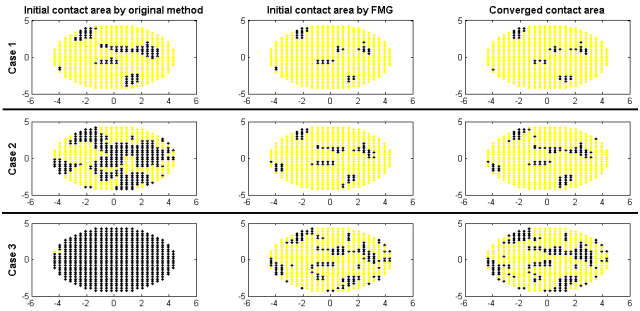

Figure 11. Rough contact: contact area on a 32×32 grid for Cases 1, 2 and 3. The first column: the initial contact area obtained by the original method, selecting all the elements I with $h_I \leq 0$; the second column: the initial contact area by the FMG scheme; the last column: the converged contact area.

turns out that, the strategy to obtain the initial contact area is efficient even when the area is irregular.

6 Conclusions

In this paper we presented a full multigrid method, which is a combination of a multigrid method, an active set algorithm and the nested iteration approach, to solve linear complementarity problems arising from elastic normal contact problems.

Multigrid using damped GS smoother is efficient for solving the corresponding integral equations, that give rise to a dense coefficient matrix. One multigrid cycle within an active set iteration appears to be sufficient to give an approximate solution to modify the contact areas efficiently and accurately. In particular, we do not only restrict the defects but also the contact area, and we set quantities outside the contact area equal to zero.

The FMG scheme provides accurate initial pressures when solving system (2.11), and also a highly satisfactory initial contact area, resembling the converged contact area much better than the initial contact area in the original method. The number of active set iterations and work units by FMG stays stable or even decreases as the problem size gets larger. Moreover, the FMG method achieves discrete error accuracy in a few iterations on the target grid.

According to the results for the rough surface contact, the FMG method shows robustness for the LCP on irregular computational domains. This is different from [23], which indicates a difficulty of FMG for rough contact problems since the coarse grid could not represent the roughness well. In our FMG similar rough surfaces are generated on the successive grids.

The GS method is not a simultaneous displacement relaxation, hence a fast computing technique for MVPs, such as FFT computations or MLMI, can not be applied. A preconditioner based on the FFT has been applied to the CG solver for contact problems in [33]. This preconditioner has been studied as a smoother in a multigrid method for a 2D simplified frictional contact problem

in [40], where a Toeplitz matrix was solved. Our future work is to extend the FFT smoother for 3D problems, which requires to solve BTTB matrices.

Acknowledgements

Jing Zhao is grateful for the financial support by the China Scholarship Council (CSC).

Appendix: generation of rough surface

Contact surfaces are not smooth for most cases in real life. Hence, we also study the normal contact problems, where rough surfaces are involved. Our interest in rough surfaces stems from railway applications [4, 14]. First of all, the influence of roughness on the creep force curve is desired. Secondly, the real stresses between railway wheels and rails are needed for assessing wear and material damage phenomena. In the numerical experiments, we will focus on friction-less rough elastic contact problems that have been studied by Greenwood, Williamson [9] and Johnson [12].

A rough surface has to be generated when studying rough surface contact. It is regarded here as a random process, characterized by a height distribution and an auto-correlation function (ACF), which defines the correlation between two points at the surface. Patir [19] defined a method to generate a random surface whose height is Gaussian distributed: a linear transformation was made on a random matrix to obtain the surface height where the given ACF was used to determine the amplitudes for each random component. Hu and Tonder [10] used finite impulse response (FIR) filters for the generation of rough surfaces. They regarded this procedure as input Gaussian distributed signals passing through a FIR filter. Their method was considered not highly satisfactory in [37], in which another approach based on the fast Fourier transform (FFT) for the generation was proposed. Besides Gaussian rough surfaces, the generation of non-Gaussian rough surfaces is also studied, for example by Patir [19], Wu [38], amongst others.

We would like to discuss a method, based on [14], to generate Gaussian rough surfaces, where the standard deviation of the surface heights σ is given.

The formula in [14] for the surface height $z(x, y)$ on a rectangle $[0, l_x] \times [0, l_y]$ is a randomized version of the two-dimensional wavy surface given by Johnson [12], which we write as:

$$z(x,y) = \sum_{m=1}^{M} \sum_{n=1}^{N} a_{mn} \cos\Big(\frac{2\pi m x}{l_x} + \varphi_{mn}\Big) \cos\Big(\frac{2\pi n y}{l_y} + \theta_{mn}\Big), \tag{6.1}$$

where each frequency pair (m, n) has phases φ_{mn} and θ_{mn}, that are uniformly distributed on $[0, 2\pi]$, amplitude a_{mn} is uniformly distributed on $[0, A_{mn}]$ and, here, $A_{mn} := A \cdot \gamma^{m+n-2}$ with A a reference amplitude. The decay factor γ satisfies $0 < \gamma \leq 1$. The choices for M, N and γ in this model are flexible and when $M = N = 1$ this results in a wavy surface.

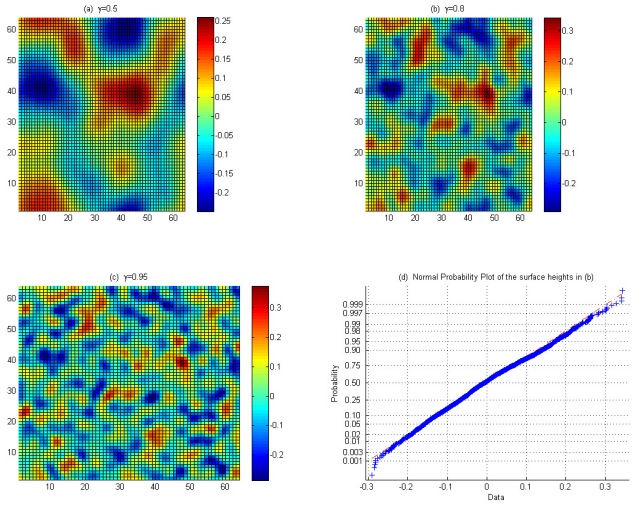

Figure 12. Rough surfaces on $[-6,6]\times[-5,5]$ mm^2 with $\sigma=0.1$: (a) $\gamma=0.5$; (b) $\gamma=0.8$; (c) $\gamma=0.95$; (d) The normal plot of the surface heights in (b).

The expression for the auto-correlation function $R(x,y)$ of the surface height in [14] can be written as:

$$R(x,y)=\frac{1}{4}\sum_{m=1}^{M}\sum_{n=1}^{N}a_{mn}^2\cos\Big(\frac{2\pi mx}{l_x}\Big)\cos\Big(\frac{2\pi ny}{l_y}\Big).$$

Then, $R(0,0)$ is equal to σ^2, i.e.:

$$R(0,0)=\sigma^2=\frac{1}{4}\sum_{m=1}^{M}\sum_{n=1}^{N}a_{mn}^2. \tag{6.2}$$

We would like to calculate the surface height z, when σ is given. A random number generator is used to obtain φ_{mn} and θ_{mn} for each frequency pair (m,n). The determination of the amplitude a_{mn} requires the value of the reference amplitude A, which is chosen to be 1, and then the true amplitudes are scaled in accordance with the desired standard deviation σ. This can be done by the following steps:

1. Obtain random coefficients $\tilde{a}_{mn}$ uniformly distributed on $[0,\gamma^{m+n-2}]$ by a random number generator.
2. Calculate the auto-correlation, which is denoted by $\tilde{R}(0,0)$, using $\tilde{a}_{mn}$ with equation (6.2).
3. Scale the coefficients $\tilde{a}_{mn}$ by a factor $\frac{\sigma}{\sqrt{\tilde{R}(0,0)}}$, i.e. $a_{mn}=\tilde{a}_{mn}\frac{\sigma}{\sqrt{\tilde{R}(0,0)}}$.

After the amplitudes a_{mn} are obtained, formula (6.1) will give the surface heights at the positions (x,y).

To test this rough surface generation technique, we generate rough surfaces on $[-6,6]\times[-5,5]$ mm^2 with $\sigma = 0.1$. A 64^2-grid is used for the discretization and we choose $M = 12, N = 10$ in (6.1). Fig. 12 displays the resulting rough surfaces with $\gamma = 0.5$, 0.8 and 0.95 in (a) (b) and (c), respectively. We find that the surface heights of these three rough surfaces having zero mean and the desired standard deviation being $\sigma = 0.1$. In Fig. 12(d), a normal probability plot of the surface heights of Fig. 12(b) indicates that the surface heights are well Gaussian distributed (since the values are very close to the red straight line which represents the Gaussian distribution). We also generated surfaces for different values for M and N, and found that large values of M and N will result in better Gaussian distributed surface heights. We can always achieve the desired standard deviation σ, independent of the values of M and N.

Comparing the three different rough surfaces in Fig. 12, we see that as γ increases, more peaks will be found on the corresponding rough surface. This implies that increasing the value of γ leads to a larger *asperity density*, as is introduced in [12].

References

[1] T. Andersson. The boundary element method applied to two-dimensional contact problems with friction. In *Proceedings of the 3rd International Seminar on Recent Advances in Boundary Element Methods*. Springer, Berlin, 1981.

[2] A. Brandt and C.W. Cryer. Multigrid algorithms for the solution of linear complementarity problems arising from free boundary problems. *SIAM J. Sci. Statist. Comput.*, **4**(4):655–684, 1983. http://dx.doi.org/10.1137/0904046.

[3] A. Brandt and A.A. Lubrecht. Multilevel matrix multiplication and fast solution of integral equations. *J. Comput. Phys.*, **90**(2):348–370, 1990. http://dx.doi.org/10.1016/0021-9991(90)90171-V.

[4] F. Bucher, K. Knothe and A. Theiler. Normal and tangential contact problem of surfaces with measured roughness. *Wear*, **253**(1):204–218, 2002. http://dx.doi.org/10.1016/S0043-1648(02)00102-3.

[5] R.H.F. Chan and X.Q. Jin. *An Introduction to Iterative Toeplitz Solvers*. SIAM, 2007.

[6] R. Enblom. Deterioration mechanisms in the wheel–rail interface with focus on wear prediction: a literature review. *Vehicle Syst. Dyn.*, **47**(6):661–700, 2009. http://dx.doi.org/10.1080/00423110802331559.

[7] S.L. Grassie. Rolling contact fatigue on the British railway system: treatment. *Wear*, **258**(7):1310–1318, 2005. http://dx.doi.org/10.1016/j.wear.2004.03.065.

[8] R.M. Gray. *Toeplitz and Circulant Matrices: A Review*. Now Publisher Inc., 2006.

[9] J.A. Greenwood and J.B.P. Williamson. Contact of nominally flat surfaces. *Proc. R. Soc. Lond. Ser. A Math. Phys. Sci.*, **295**(1442):300–319, 1966.

[10] Y.Z. Hu and K. Tonder. Simulation of 3-D random rough surface by 2-D digital filter and Fourier analysis. *Int. J. Mach. Tools Manufact.*, **32**(1):83–90, 1992. http://dx.doi.org/10.1016/0890-6955(92)90064-N.

[11] T. Huckle. Circulant and skew circulant matrices for solving Toeplitz matrix problems. *SIAM J. Matrix Anal. A*, **13**(3):767–777, 1992. http://dx.doi.org/10.1137/0613048.

[12] K.L. Johnson. *Contact Mechanics*. Cambridge University Press, 1985.

[13] J.J. Kalker. *Three-Dimensional Elastic Bodies in Rolling Contact*. Kluwer Academic Publisher, 1990.

[14] J.J. Kalker, F.M. Dekking and E.A.H. Vollebregt. Simulation of rough, elastic contacts. *Trans. ASME, J. Appl. Mech.*, **64**(2):361–368, 1997. http://dx.doi.org/10.1115/1.2787315.

[15] N. Kikuchi and J.T. Oden. *Contact Problems in Elasticity: A Study of Variational Inequalities and Finite Element Methods*. SIAM, 1987.

[16] R. Krause. A nonsmooth multiscale method for solving frictional two-body contact problems in 2D and 3D with multigrid efficiency. *SIAM J. Sci. Comput.*, **31**(2):1399–1423, 2009. http://dx.doi.org/10.1137/070682514.

[17] K.W. Man. *Contact Mechanics Using Boundary Elements*. Computational Mechanics Publisher, 1994.

[18] K.G. Murty. *Linear Complementarity, Linear and Nonlinear Programming*. Heldermann Berlin, 1988.

[19] N. Patir. A numerical procedure for random generation of rough surfaces. *Wear*, **47**(2):263–277, 1978. http://dx.doi.org/10.1016/0043-1648(78)90157-6.

[20] I.A. Polonsky and L.M. Keer. A numerical method for solving rough contact problems based on the multi-level multi-summation and conjugate gradient techniques. *Wear*, **231**(2):206–219, 1999. http://dx.doi.org/10.1016/S0043-1648(99)00113-1.

[21] V.L. Popov. *Contact Mechanics and Friction: Physical Principles and Applications*. Springer, 2010.

[22] E. Rabinowicz. *Friction and Wear of Materials*, volume 2. Wiley, 1995.

[23] P. Sainsot and A.A. Lubrecht. Efficient solution of the dry contact of rough surfaces: a comparison of fast Fourier transform and multigrid methods. *Proc. Inst. Mech. Eng. Part J: J. Eng. Tribology*, **225**(6):441–448, 2011. http://dx.doi.org/10.1177/1350650111401535.

[24] H. Schippers. Multigrid methods for boundary integral equations. *Numer. Math.*, **46**(3):351–363, 1985. http://dx.doi.org/10.1007/BF01389491.

[25] H.M. Stanley and T. Kato. An FFT-based method for rough surface contact. *ASME J. Tribol.*, **119**(3):481–485, 1997. http://dx.doi.org/10.1115/1.2833523.

[26] G. Strang. A proposal for Toeplitz matrix calculations. *Stud. Appl. Math.*, **74**(2):171–176, 1986.

[27] U. Trottenberg, C.W. Oosterlee and A. Schüller. *Multigrid*. Academic Press, 2000.

[28] A. van Beek. *Advanced Engineering Design: Lifetime Performance and Reliability*. Delft University of Technology, 2006.

[29] C.H. Venner and A.A. Lubrecht. *Multi-Level Methods in Lubrication*. Elsevier Science, 2000.

[30] C.H. Venner and W.E. Napel. Multilevel solution of the elastohydrodynamically lubricated circular contact problem, Part I: Theory and numerical algorithm. *Wear*, **152**(2):351–367, 1992. http://dx.doi.org/10.1016/0043-1648(92)90132-R.

[31] E.A.H. Vollebregt. The bound-constrained conjugate gradients method for non-negative matrices. *J. Optim. Theory Appl.*, 2013. http://dx.doi.org/10.1007/s10957-013-0499-x.

[32] E.A.H. Vollebregt. User's guide for CONTACT, Vollebregt & Kalker's rolling and sliding contact model. Technical Report TR09-03, version 13.1, VORtech, The Netherlands, 2013.

[33] E.A.H. Vollebregt. A new solver for the elastic normal contact problem using conjugate gradients, deflation, and an FFT-based preconditioner. *J. Comput. Phys.*, **257**:333–351, 2014. http://dx.doi.org/10.1016/j.jcp.2013.10.005.

[34] E.A.H. Vollebregt and H.M. Schuttelaars. Quasi-static analysis of two-dimensional rolling contact with slip-velocity dependent friction. *J. Sound. Vib.*, **331**(9):2141–2155, 2012. http://dx.doi.org/10.1016/j.jsv.2012.01.011.

[35] T. von Petersdorff and E.P. Stephan. Multigrid solvers and preconditioners for first kind integral equations. *Numer. Meth. Part. D. E*, **8**(5):443–450, 1992. http://dx.doi.org/10.1002/num.1690080504.

[36] P. Wriggers. *Computational Contact Mechanics*. Springer-Verlag, 2006.

[37] J.J. Wu. Simulation of rough surfaces with FFT. *Tribol. Int.*, **33**(1):47–58, 2000. http://dx.doi.org/10.1016/S0301-679X(00)00016-5.

[38] J.J. Wu. Simulation of non-gaussian surfaces with FFT. *Tribol. Int.*, **37**(4):339–346, 2004. http://dx.doi.org/10.1016/j.triboint.2003.11.005.

[39] J. Zhao, E.A.H. Vollebregt and C.W. Oosterlee. A full multigrid method for linear complementarity problems arising from elastic normal contact problems. Student competition paper for the 12th Copper Mountain conference, USA, 2012.

[40] J. Zhao, E.A.H. Vollebregt and C.W. Oosterlee. Multigrid with FFT smoother for a simplified 2D frictional contact problem. *Numer. Linear Algebra Appl.*, **21**(2):256–274, 2014. http://dx.doi.org/10.1002/nla.1923.